Microglia remodel the synaptic signaling required for context-dependent cognitive performance

Renato Socodato[1,*,#], Tiago O. Almeida[1,9*], Camila C. Portugal[1], Evelyn C. S. Santos[1], Joana Tedim-Moreira[1], Teresa Canedo[1,5], Filipa I. Baptista[4], Ana Magalhães[1], António F. Ambrósio[4], Cord Brakebusch[8], Boris Rubinstein[6], Irina Moreira[7], Teresa Summavielle[1,2], Inês Mendes Pinto[1,3] and João B. Relvas[1,5,#]

[1]Institute of Research and Innovation in Health (i3S) and Institute for Molecular and Cell Biology (IBMC), University of Porto, Porto, Portugal.

[2]ESS.PP, Escola Superior de Saúde do Politécnico do Porto, Porto, Portugal.

[3]International Iberian Nanotechnology Laboratory (INL), Braga, Portugal.

[4]Center for Innovative Biomedicine and Biotechnology (CIBB), Coimbra Institute for Clinical and Biomedical Research (iCBR), and Clinical Academic Center of Coimbra (CACC), University of Coimbra, Coimbra, Portugal.

[5]Faculty of Medicine of the University of Porto (FMUP), Porto, Portugal.

[6]Stowers Institute for Medical Research; Kansas City, MO, USA.

[7]Department of Life Sciences, Center for Innovative Biomedicine and Biotechnology (CIBB) and CNC-Center for Neuroscience and Cell Biology, University of Coimbra, Coimbra, Portugal.

[8]Molecular Pathology Section, BRIC, Københavns Biocenter, Copenhagen, Denmark.

[9]ICBAS - School of Medicine and Biomedical Sciences, Porto, Portugal.

[*]Equally contributed to this work.

[#]Correspondence to: renato.socodato@ibmc.up.pt or jrelvas@ibmc.up.pt

Abstract

Microglia modulate synaptic activity, essential for context-dependent cognitive performance, allowing organism-level adaptations to different environmental scenarios. Yet, the microglial molecular drivers required for synaptic remodeling related to cognitive performance remain largely elusive. Here, combining conditional gene targeting, single-cell live imaging, RNA-seq, high-throughput proteomics, systems biology, and animal behavior, we mapped a molecular nexus between microglia and synapses that instructs cognitive performance. Specifically, we found that microglia use the RhoGTPase Rac1 as a relay switch to sense the brain microenvironment and drive synaptic remodeling required for experience-dependent sociability and learning related to memory. Targeting this microglial relay modifies context-dependent cognitive performance.

Introduction

Microglia, the largest myeloid cell population in the CNS, are best known for their protective roles in the brain. Not only are microglia involved in physiological synaptic pruning, but they also secrete a plethora of chemical mediators that broadly impact brain function (*1*). Targeted gene ablation experiments indicate that microglia-secreted factors (secretome) are putative modulators of synaptic activity and plasticity (*2-5*). Even though the microglial secretome conceivably regulates many aspects of microglia-synapse crosstalk, little is known about the magnitude and specificity of the alterations in synaptic signaling and remodeling elicited by the chemical mediators secreted by microglia (*6*).

Remodeling of the synaptic structure and signaling, bona fide synaptic plasticity modalities, occurs continuously throughout life and underlies high-order cognitive functions necessary for an organism to cope with different environmental scenarios (*7*). Thus, deciphering how the brain encodes and stores experiences triggered by different environmental contexts requires in-depth knowledge of the cellular and molecular mechanisms governing synaptic remodeling, including those in which microglia participate.

Here, we reveal that the conditional ablation of the small RhoGTPase Rac1 in adult microglia suppresses their ability to read and interpret cues from the brain microenvironment, severing microglial cells' capacity to communicate with synapses properly. Loss of homeostatic microglia-to-synapse communication primarily disrupted the signaling remodeling of synapses required for experience-dependent plasticity, impairing context-dependent learning, memory, and sociability.

Results

A RhoGTPase relay connects microglia with synapses

The GTPases of the Rho family, including the most well-characterized members Rac1, RhoA, and Cdc42, are critical orchestrators of cellular homeostasis (*8*). Accordingly, we have reported that RhoA is a critical negative regulator of microglia immune activity causing neurodegeneration (*4*). Here, to understand microglia-to-synapse communication in the adult brain, we disrupted microglia homeostasis by genetically targeting Rac1. Thus, we crossed Cx3cr1$^{CreER\text{-}IRES\text{-}EYFP}$ mice (*3, 9, 10*) with mice carrying Rac1 floxed alleles (*11*) (**Suppl. Fig. 1A**). Following tamoxifen administration, Cre migrates to the nucleus inducing conditional Rac1 gene inactivation in microglia from Cx3cr1^{CreER+}:Rac1$^{fl/fl}$ mice. Analysis by flow cytometry (gating strategy in **Suppl. Fig. 1B**) and qRT-PCR showed, as expected, a robust decrease of Rac1 in Cx3cr1^{CreER+}:Rac1$^{fl/fl}$ microglia (**Fig. 1A** and **Suppl. Fig. 1C**, respectively). While Cx3cr1^{CreER+} mice have only one intact copy of the Cx3cr1 allele, haploinsufficiency had no impact on Rac1 expression in Cx3cr1^{CreER+} microglia (**Fig. 1A**).

To show that microglial Rac1 directly impacts microglia-to-synapse communication, we looked for global effects in synaptic structure and density. We found that the brains of Cx3cr1^{CreER+}:Rac1$^{fl/fl}$ mice had reduced spine density (**Fig. 1B**) and decreased excitatory (PDS-95^{+}/vGlut1^{+}) synapse number (**Fig. 1C**). The decrease in the numbers of spines and excitatory synaptic puncta caused by disrupting microglia-to-synapse communication should alter cognitive function, including learning and memory. Thus, we used the Morris Water Maze (MWM) test to evaluate learning and memory. Indeed, Cx3cr1^{CreER+}:Rac1$^{fl/fl}$ mice had a significant delay finding the hidden platform in the learning phase (**Fig. 1D**) and spent significantly less time in the target quadrant in the probe trial (**Fig. 1E**). We concluded that disrupting homeostatic microglia-to-synapse communication leads to synaptic structural changes that correlate with deficits in learning and memory.

Mapping the molecular nexus between microglia and synapses

To elucidate putative microglial signaling pathways correlated to synapse number, learning, and memory deficits, we conducted RNA-seq analysis in Cx3cr1^{CreER+}:Rac1$^{fl/fl}$ and Rac1$^{fl/fl}$ microglia. After microglial isolation and sequencing, we performed pre-ranked gene set enriched analysis (GSEA) and String Ranked Enrichment (SRE) (**Suppl. Fig. 1D** and **Suppl. Table 1**). Contingency analyses (**Suppl. Fig. 2A**) using known microglial functional modules (including homeostatic (*12*), pro-inflammatory (*13*), oxidative stress (*14*), disease-associated (*15*), injury-related (*16*), and aging (*16*)) showed no significant association with Rac1-regulated DEGs (differentially expressed genes) (**Suppl. Table 1)**. Manual trimming and analogy recategorizing relevant pathways to build logical signaling modalities led to the classification of two microglial transcriptomic programs potentially associated with synaptic function and behavior: microglial environmental sensing (**Suppl. Fig. 1E**) and microglia-synapse crosstalk (**Suppl. Fig. 1F**).

The microglial environmental sensing program included two modules: cell cycle regulation and innate immune signaling (**Suppl. Fig. 1E** and **Suppl. Table 2**). We confirmed some of the transcripts' altered expression related to microglia immune signaling by qRT-PCR in flow cytometry-sorted microglia (**Suppl. Fig. 2B**). Then, we functionally validated that Rac1 operated as a relay for microglial sensing of external cues in vitro (**Suppl. Fig. 3A-F** and **Suppl. Table 3**) and in vivo (**Suppl. Fig. 3G-I**).

The microglia-synapse crosstalk program also included two modules: intracellular protein trafficking, sorting, and export/secretion, and ECM/Growth factor signaling (**Suppl. Fig. 1F** and **Suppl. Table 4**). The protein trafficking/export/secretion module included pathways related to Rab-dependent protein trafficking and cargo flux through microglial endomembranes. The ECM/Growth factor signaling module included pathways related to adhesion/extracellular matrix (ECM), GDNF/NCAM-dependent pathway, EPH-ephrin signaling, and, as expected, synaptic function (**Suppl. Fig. 1F** and **Suppl. Table 4**). Glial cell-derived neurotrophic factor (GDNF) interacts with the neuronal ECM (via NCAMs) (*17*) and ephrins (*18*) to modulate synapse formation and plasticity (*19-21*), and is sorted in and

secreted from vesicles enriched in Rab GTPases (*22*), specifically the Rab27/3 family branch (*23*). We used Rab27a (a microglia-enriched Rab) and GDNF as functional readouts to corroborate the transcriptomic data related to protein trafficking/sorting and growth factor signaling in Rac1 mutant microglia. Indeed, we found the Rab27a/GDNF axis to be a putative downstream target of Rac1 in microglia (**Suppl. Fig. 4A-J**). In agreement with a growth factor-associated mechanism modulating homeostatic microglia-to-synapse communication, neither reduced neuronal cell numbers (**Suppl. Fig. 5A**) nor increased pruning of excitatory synapses (**Suppl. Fig. 5B**) nor neuroinflammation (**Suppl. Fig. 5C**) was sufficient to explain the decrease in spine density/synapse numbers found in Cx3cr1^{CreER+}:Rac1$^{fl/fl}$ brains.

To understand the modifications in the synaptic signaling elicited by microglia, we conducted quantitative high-throughput proteomics and phosphoproteomics in synaptosomal preparations from the brains of Cx3cr1^{CreER+}:Rac1$^{fl/fl}$ and Rac1$^{fl/fl}$ mice (**Fig. 1F**). Label-free quantification (LFQ) identified 4641 unique proteins from which 126 had their abundances differentially expressed (DE), comparing the proteomes of Cx3cr1^{CreER+}:Rac1$^{fl/fl}$ and Rac1$^{fl/fl}$ synaptosomes (**Suppl. Table 5**). Moreover, phosphoproteomics analysis identified 4389 phosphopeptides, from which 210 (corresponding to 167 unique proteins) were significantly altered between Cx3cr1^{CreER+}:Rac1$^{fl/fl}$ and Rac1$^{fl/fl}$ synaptosomes (**Suppl. Table 6**).

To interrogate the synaptic protein network regulated by microglia, we developed functional similarity matrices (**Fig. 1G** and **H**), allowing direct global analysis of similarity alterations in the proteome structure of Cx3cr1^{CreER+}:Rac1$^{fl/fl}$ and Rac1$^{fl/fl}$ synaptosomes. We found 2 enriched Cellular Component ontology terms for Cx3cr1^{CreER+}:Rac1$^{fl/fl.}$ and 7 for Rac1$^{fl/fl}$ synaptosomes. GO:0045202 (synapse) and GO:0098793 (presynapse), common to Cx3cr1^{CreER+}:Rac1$^{fl/fl}$ and Rac1$^{fl/fl}$ mice, showed a higher similarity and differentiated themselves for the other postsynaptic clusters (**Fig. 1G**). We also found 13 unique proteins within Rac1$^{fl/fl}$ proteome and 5 within Cx3cr1^{CreER+}:Rac1$^{fl/fl}$ proteome and constructed a comparable similarity matrix for the DE synaptosomal proteins (**Fig. 1H**). These results indicate a substantial loss of functional modular polarization in the synaptic proteome of Cx3cr1^{CreER+}:Rac1$^{fl/fl}$ mice.

Then, we used an ontology-based pipeline (**Fig. 1F**) to map the synaptic signaling regulated by microglia. Network clustering segregated each synaptic compartment into three distinct functional modules (**Fig. 1I**). Whereas the presynaptic modules regulated by microglia included neurotransmitter release, presynaptic AMPA receptors, lysophospholipid/sphingosine 1-phosphate receptor, erythropoietin, and interleukin signaling, the postsynaptic modules included AMPA receptor activation and synaptic plasticity, NMDA-depended Camk2/CREB activation, and ECM/growth factor regulation of synaptic signaling. Various synaptic proteins altered in a microglia-dependent manner were common to both pre and postsynaptic compartments (**Suppl. Fig. 6** and **Suppl. Table 7**), including the major integrators Camk2a, Gria2, Efnb3, and Gephyrin (Gphn). Synaptic proteins regulated by microglia exclusive to the presynaptic network included the synaptic vesicle fusion regulator Doc2a, and the modulators of presynaptic vesicle clustering/cycling/priming Stxbp5, Sv2a, Syn1, Nsf, Rph3a, Bsn, and Pclo (**Suppl. Fig. 6** and **Suppl. Table 7**). Synaptic proteins regulated by microglia exclusive to the postsynaptic network included the critical postsynaptic scaffolds/organizers Shank3, Ctnnd2, PSD-93, Sptbn1, and Nrgn, and the critical synaptic activity integrators, DARPP-32, Rgs14, and Erk2 (**Suppl. Fig. 6** and **Suppl. Table 7**).

Altogether, these results raise the hypothesis that synaptic remodeling requires microglia. To test this hypothesis, we incubated primary cortical neurons with conditioned media obtained from control (scrambled MCM) or Rac1-deficient (Rac1 KD MCM) microglia and evaluated single-spine actin cytoskeleton and Ca^{2+} dynamics during activity-dependent spine remodeling (**Suppl. Fig. 7A**). Single-spine Ca^{2+} imaging (using the Ca^{2+} sensor GCaMP6f) revealed largely different kinetics of activity-dependent Ca^{2+} increase between scrambled MCM spines (**Suppl. Fig. 7B;** 1/slope = 595 au.s^{-1}) and Rac1 KD MCM spines (**Suppl. Fig. 7B;** 1/slope = 2099 au.s^{-1}). Such different time-dependent kinetics correlated with higher (**Fig. 1J** and **Suppl. Fig. 7C**) and faster (**Fig. 1K** and **Suppl. Fig. 7C**) activity-

dependent Ca^{2+} responses in Rac1 KD MCM spines, indicating that loss of Rac1 signaling in microglia leads to aberrant spine Ca^{2+} overload during synaptic activity.

It is widely accepted that spine Ca^{2+} dynamics modulate spine structural changes. Thus, we investigated the remodeling of scrambled MCM spines and Rac1 KD MCM spines during synaptic activity. In both conditions, the overall dynamics of activity-dependent spine remodeling were similar (**Suppl. Fig 7D**), with an initial fast and transitory spine enlargement alongside actin polymerization followed by sustained spine contraction paralleled by actin depolymerization. However, the kinetics of activity-dependent remodeling varied substantially between scrambled MCM spines and Rac1 KD MCM spines (**Fig. 1L and M** and **Suppl. Fig 7E-N**). Specifically, Rac1 KD MCM spines grew bigger and faster during the enlargement phase (**Fig. 1L** and **Suppl. Fig. 7E**). Rac1 KD MCM spines also shrank more and faster during the contraction phase (**Fig. 1M** and **Suppl. Fig. 7F**).

Furthermore, in scrambled MCM spines, the activity-dependent spine enlargement and spine actin polymerization were desynchronized (**Suppl. Fig. 7G**), whereas transitory spine enlargement was associated positively with spine Ca^{2+} increase (**Suppl. Fig. 7H**). Thus, the activity-dependent transitory enlargement of scrambled MCM spines depended largely on Ca^{2+}-associated membrane elasticity and not actin cytoskeleton elongation, which is in line with an actin polymerization-independent mechanism for transitory spine enlargement during synaptic activity in hippocampal slices (*24*). However, in Rac1 KD MCM spines, both activity-dependent actin polymerization and Ca^{2+} increase positively associated with abnormal spine enlargement (**Suppl. Fig. 7I and J**), indicating that the lack of microglial Rac1 relay caused aberrant spine enlargement through Ca^{2+} overload.

Moreover, the association of Ca^{2+} and actin dynamics with activity-dependent spine contraction also differed markedly between scrambled MCM spines and Rac1 KD MCM spines (**Suppl. Fig. 7K-N**). In scrambled MCM spines, actin depolymerization and Ca^{2+} increase positively associated with activity-dependent spine contraction (**Suppl. Fig. 7K and L**), showing that, in normal conditions, spine Ca^{2+} increase during synaptic activity promotes spine shrinkage by driving actin depolymerization. The more significant and faster spine contraction found in Rac1 KD MCM spines during synaptic activity associated positively with actin depolymerization (**Suppl. Fig. 7M**) but not with spine Ca^{2+} dynamics (**Suppl. Fig. 7N**), suggesting that the initial Ca^{2+} overload in Rac1 KD MCM spines also drives disproportionate actin depolymerization leading to excessive spine shrinkage during synaptic activity. These data indicate that microglia modulate synaptic remodeling triggered by neuronal activity.

<u>Microglia-synapse nexus instructs context-dependent cognitive performance</u>

Microglia modulated the steady-state synaptic signaling, but could microglia also impact the remodeling of synaptic signaling driven by experience? Experience-dependent remodeling is the capacity of synapses to change and adapt to environmental inputs and learning (*25*) and relies on multistep phosphorylation of synaptic proteins (*26*). Thus, we used the environmental enrichment (EE) paradigm, which relates to improving sensory, motor, and cognitive stimulation in the housing conditions, to drive context-dependent synaptic remodeling. Then, we used quantitative phosphoproteomics in hippocampal synaptosomal preparations obtained from $Rac1^{fl/fl}$ and $Cx3cr1^{CreER+}$:$Rac1^{fl/fl}$ mice housed under EE or control environment (CE) (**Fig. 2A**) to elucidate changes in the remodeling of the synaptic signaling modulated by microglia.

After unbiased high-confidence mapping, we found that the synaptic phosphoproteome driven by EE featured modifications in the abundance of 622 phosphopeptides (out of 3602), of which 298 emerged specifically during EE, with upregulation of other 303 and downregulation of 21 phosphopeptides, corresponding to 390 phosphoproteins (**Fig. 2B**). To extract consensual information related explicitly to synaptic pathways, we used ORA with the 390 matched phosphoproteins and found that EE significantly modified over 600 biological processes, 152 molecular functions, and 206 cellular components in the synapses (**Fig. 2B** and **Suppl. Table 8**). Pre and postsynapse organization, SNARE complex assembly, secretion of neurotransmitters, GABA and

glutamate-dependent synaptic signaling, and postsynaptic cytosolic calcium levels were among the top signaling pathways modulated by EE in Rac1$^{fl/fl}$ hippocampus (**Suppl. Fig. 8A** and **Suppl. Table 8**). Unbiased PPI clustering identified five distinct phosphoprotein hubs comprising the EE-driven synaptic phosphoproteome (**Suppl. Fig. 8B**).

We then used set theory to segregate the 390 synaptic phosphoproteins into two functional modules regulated by EE (**Fig. 2C** and **Suppl. Table 9**): one utterly independent of microglia (138 phosphoproteins) and another strictly modulated by microglia (149 phosphoproteins). Coalescing ORA and gene ontology allowed us to map the experience-dependent synaptic signaling modules exclusively related to microglia (**Fig. 2D** and **Suppl. Table 9**).

Specifically, global neurotransmitter release/recycle mechanisms, spine maintenance, postsynaptic architecture, excitatory neurotransmission, and regulation of actin nucleation were the most representative pathways modulated by EE through microglia (**Fig. 2D** and **Suppl. Table 9**). On the other hand, synaptic protein trafficking, endocannabinoid-dependent trans-synaptic signaling, glutamate/dopamine metabolism, GABA-dependent neurotransmission, and regulation of microtubule polymerization were among the top representative pathways controlled by EE independently of microglia (**Suppl. Fig. 8C**).

To provide further mechanistic insight into how microglia-dependent regulation of dynamic phosphorylation events was connected to synaptic function (for instance, neurotransmitter release and excitatory postsynaptic activity) during experience-dependent plasticity, we focused on the prominent synaptic integrator Camk2. After sequence analysis and literature curation, we identified a context- and microglia-dependent Camk2 circuitry operating simultaneously at both synaptic compartments (**Fig. 2E**). We detected hyperphosphorylation of canonical T286 in Camk2a and T287 in Camk2b, both known to induce kinase activation, in a microglia-regulated manner. Increased phosphorylation of S330, known to control binding to Camk2b, Camk2d, and Camk2g, was also modulated by microglia. At the presynapse, microglia-mediated overactivation of Camk2a most likely disarrayed the fusion machinery for neurotransmitter release (composed of increased phosphorylated forms of Syt7 and Vamp4 and their synaptic partners), leading to an aberrant increase of neurotransmitter release (**Fig. 2E**). At the postsynapse, microglia-mediated overactivation of Camk2a, elicited by hyperactivity of GluN2B-containing NMDA receptors (hyperphosphorylated at S1303) and derangements of PSD scaffolds (illustrated by decreased phosphorylation of Shank1, 2, and 3), likely compromised the integration of postsynaptic potentials leading to deficits in excitatory neurotransmission (**Fig. 2E**). Here we concluded that microglia modulate the remodeling of the synaptic signaling during experience-dependent plasticity.

Dynamic remodeling of protein phosphorylation networks is critical for cognitive function (27). So, we postulated that by modulating the remodeling of the synaptic signaling, microglia should also impact context-dependent cognitive performance. In such a way, we conducted different behavioral tests to evaluate the enhancement of the cognitive performance in Rac1$^{fl/fl}$ and Cx3cr1^{CreER+}:Rac1$^{fl/fl}$ mice housed under EE or CE (**Fig. 2F**).

First, we assessed contextual memory in the step-down passive avoidance test (*28*). Using 3-Way ANOVA, we found, as expected, that the step-down latency was significantly higher in the test session than in the training session (**Fig. 2G**). Multiple comparisons within 3-Way ANOVA revealed an intergroup variation in memory recall (test session latency; **Fig. 2G**), suggesting that EE and CE might have affected memory retention differently across genotypes. Indeed, using a retention index transformation, we found that EE significantly increased retention in Rac1$^{fl/fl}$ mice (**Fig. 2H**), whereas ablating microglial Rac1 abolished the EE-induced improvement in memory retention (**Fig. 2H**).

Second, we used the novel object recognition (NOR) test to evaluate recognition memory (*29*) in Rac1$^{fl/fl}$ and Cx3cr1^{CreER+}:Rac1$^{fl/fl}$ mice housed under EE or CE. We found that EE increased the degree of novel object exploration (**Fig. 2I**) and the discrimination of the novel object over the familiar object (**Fig. 2J**) in Rac1$^{fl/fl}$ mice, indicating that EE

improved recognition memory. On the other hand, the EE-induced improvement in the NOR performance was blocked entirely in Cx3cr1^{CreER+}:Rac1$^{fl/fl}$ mice (**Fig. 2I** and **J**).

Third, we used the Y-maze test to evaluate working memory (*30*) in Rac1$^{fl/fl}$ and Cx3cr1^{CreER+}:Rac1$^{fl/fl}$ mice housed under EE or CE. We found that EE significantly decreased the number of arm entry errors, or incorrect arm returns, during the spontaneous maze alternation in Rac1$^{fl/fl}$ mice (**Fig. 2K**), indicating that EE improves spatial working memory. However, the number of wrong arm returns was comparable between EE and CE in Cx3cr1^{CreER+}:Rac1$^{fl/fl}$ mice (**Fig. 2K**). No significant differences were found in total arms entries between groups among the genotypes (**Fig. 2L**). Here we concluded that microglia modulate the EE enhancing effect in spatial working memory.

Lastly, we used the three-chamber social affiliation test (*31*) to evaluate social behavior in Rac1$^{fl/fl}$ and Cx3cr1^{CreER+}:Rac1$^{fl/fl}$ mice housed under EE or CE. Whereas EE significantly increased Rac1$^{fl/fl}$ mice's preference for exploring the compartment with a stranger animal, EE failed to improve social proximity choices in Cx3cr1^{CreER+}:Rac1$^{fl/fl}$ mice (**Fig. 2M**). Total exploration time was comparable among housing conditions and genotypes (**Fig. 2N**).

Overall, we concluded that by modulating the remodeling of the synaptic signaling, microglia instruct context-dependent learning, memory, and sociability.

Discussion

In this work, we identified a RhoGTPase-associated molecular nexus between microglia and synapses that directly impacts cognitive performance. Specifically, we mapped an experience-dependent remodeling of the synaptic signaling controlled by microglia required for context-dependent sociability and learning related to memory.

Microglia are critical regulators of synaptic structure, function, and plasticity. Microglia-synapse crosstalk may occur through direct physical contact between microglia and synaptic elements (*32*), microglia-mediated ECM remodeling around synapses (*2*), or activation of synaptic receptors by microglia-secreted molecules (secretome) (*3, 4*). RNA-seq profiling of Rac1-deficient microglia revealed impaired intracellular protein trafficking and secretion. Additionally, loss of microglial Rac1 did not significantly affect the number of neurons, neuroinflammation, and engulfment capacity of synaptic elements. On this basis, we reasoned that the lack of Rac1 signaling could be modifying the microglial secretome profile to induce the synaptic and behavioral deficits observed. In agreement with this hypothesis, we identified in vivo the microglial Rab27a/GDNF (linked to the RNAseq module of protein trafficking and secretion) as a putative downstream target of Rac1.

GDNF can signal through NCAM to drive spine formation and postsynaptic assembly (*20*). A postsynaptic adhesion complex formed by NCAM, βI-spectrin, and NMDA receptors recruits and activates CamK2a to modulate synapse formation (*33*). In agreement, the proteome and phosphoproteome profiling in brain synaptosomes of Rac1 mutants showed alterations in NCAM, spectrins, NMDA receptors, and CamK2a. Moreover, the substantial overlap of synaptic phosphoproteins (our datasets) and many mRNA species present at synaptic sites (e.g., CamK2a, NMDA receptor subunits, and actin cytoskeleton-related)(*34*) validates our synaptic proteome profiling and is in line with a role for microglia in modulating the neuronal transcriptome (*2*).

The fact that microglia instructed a synaptic remodeling logically suggested that microglia also impacted cognition. We provided evidence that microglia also controlled experience-dependent cognitive enhancement by remodeling the synaptic signaling. In future studies, mapping the experience-dependent proteome signature of microglia will provide a deeper understanding of how microglia shape the synaptic landscape to support cognitive performance.

Synaptic remodeling and plasticity ultimately govern the encoding and storage of new experiences in the brain, consequently dictating the behavioral adaptations to different environmental contexts. We triggered context-dependent synaptic remodeling using a paradigm of environmental enrichment (EE). It is well accepted that the molecular and cellular changes that EE produces in the brain correlate with enhanced cognitive function (*35*). Indeed, we found that control mice housed under EE displayed notorious improvements in learning, memory, and social plasticity, confirming that EE enhanced cognitive performance. However, EE failed to produce cognitive enhancement in microglial Rac1 mutants. The vast differences found in the phosphoproteome signature in hippocampal synapses of microglial Rac1 mutants at least partially explain why EE failed to function as a cognitive enhancer in these mutants. Hence, the combination of synaptic proteomics profiling and behavioral tests indicated that microglial function is required to trigger synaptic plasticity-related pathways connected to cognitive performance.

Finally, specifying the remodeling of the synaptic signaling controlled by microglia might have broad implications for devising strategies to enhance cognitive performance or compensate for the cognitive decline during aging or brain diseases.

Experimental Procedures

Animals: All mice experiments were reviewed by i3S animal ethical committee and were approved by Direção-Geral de Alimentação e Veterinária (DGAV). Animals were maintained with an inverted 12h/12h light-dark cycle and were allowed free access to food and water. Mice were housed under standardized cages and specific pathogen-free conditions. Experiments were carried out following the 3Rs ethics policy.

Conditional microglia Rac1-deficient mice: Cx3cr1$^{CreER-EYFP}$ mice were purchased from Jackson Laboratories and used as before (*4*). In such mice, the *Cx3cr1* promoter drives high expression of the CreER cassette in microglia (*3*). Mice homozygous for the *Rac1* floxed allele (*11*) were backcrossed at least ten generations and were kept at the I3S animal facility. PCR determined all genotypes on genomic DNA. Rac1 floxed mice were crossed with Cx3cr1$^{CreER-EYFP}$ mice. Progeny of interest were: Control (Rac1$^{fl/fl}$ or Cx3cr1^{CreER+}) and mutants (Rac1$^{fl/fl}$:Cx3cr1^{CreER+}). Mice (4/5-weeks-old) were given tamoxifen (5 mg *per* animal by oral gavage; 1 mg daily for five days) and then analyzed 6-8- or 18-weeks post-tamoxifen. Experiments were performed in female and male mice (unless specified otherwise), all kept on a C57BL/6 background.

Antibodies: The following antibodies were used in this study: Rac1 antibody [0.T.127] (Abcam Cat# ab33186, RRID:AB_777598; 1:250), Rab27a mouse monoclonal (M02), clone 1G7 (Abnova Cat# H00005873-M02, RRID:AB_519010; 1:200), Rab27a rabbit polyclonal (Sigma-Aldrich Cat# HPA001333, RRID:AB_1079730; 1:200), GDNF (Abcam Cat# ab18956, RRID:AB_2111379; 1:100-1:200), GFP (Abcam Cat# ab6673, RRID:AB_305643; 1:200), Iba1 (Wako Cat# 019-19741, RRID:AB_839504; 1:500), CD11b clone M1/70.15 (BD Biosciences Cat# 560456, RRID:AB_1645267; 1:100), PSD95 clone 6G6-1C9 (Thermo Fisher Scientific Cat# MA1-045, RRID:AB_325399; 1:600), vGlut1 (Synaptic Systems Cat# 135 303, RRID:AB_887875; 1:1,000), CD68 clone FA-11 (Bio-Rad Cat# MCA1957T, RRID:AB_2074849; 1:400), Fc Receptor Blocking Solution (BioLegend Cat# 156603, RRID:AB_2783137; 1:50), NeuN (Millipore Cat# MAB377, RRID:AB_2298772; 1:400), APC anti-mouse/human CD11b antibody (BioLegend Cat# 101212, RRID:AB_312795; 0.25 µg to 10^6 cells), Alexa Fluor® 647 anti-mouse/human CD11b antibody (BioLegend Cat# 101218, RRID: AB_389327; 0.25 µg to 10^6 cells), PE anti-mouse CD45 antibody (BioLegend Cat# 103106, RRID:AB_312971; 0.25 µg to 10^6 cells).

Primers: The primers used in this study were purchased from Sigma-Aldrich; their sequences are provided in **Suppl. Table 10**.

Plasmids: pFRET-HSP33 cys (RRID:Addgene_16076), IκBα-miRFP703 (RRID:Addgene_80005), Daglas-pm1 (PMID: 16990811), pcDNA-D1ER (RRID:Addgene_36325), CMV-R-GECO1 (RRID:Addgene_32444), CKAR (RRID:Addgene_14860), pLKO-empty (PMID: 28960571), pLKO-Rac1 shRNA (PMID: 28960571), pLKO-Rab27a shRNA (Sigma TRCN0000279985), scrambled-mCherry shRNA control (PMID: 28960571), mCherry-Rac1 shRNA (PMID: 28960571), pRK5-myc-Rac1-wt (RRID:Addgene_12985), pRK5-myc-Rac1-T17N (RRID:Addgene_12984), YF-Rac1(CA) (RRID:Addgene_20150), Lyn11-targeted FRB (LDR) (RRID:Addgene_20147), YFP-FKBP (YF) (RRID:Addgene_20175) pLKO.1 (Sigma), pLKO-Rab27a shRNA (Sigma), mCherry-Lifeact-7 (RRID:Addgene_54491), pGP-CMV-GCaMP6f (RRID:Addgene_40755).

Environmental enrichment protocol: Mice with 4-5 weeks of age were weighed and placed in Type III cages three days with two different housing conditions: control environment (CE) and enriched environment (EE). Littermates were randomly assigned to one of the housing conditions, with Rac1$^{fl/fl}$ and Cx3cr1^{CreER+}:Rac1$^{fl/fl}$ mice in every cage. CE only contained bedding material (corn cob, grade 12) and tissue paper. EE had bedding material, tissue paper, a small cardboard tube, four small aspen bricks, a wood ladder, a vertical plastic running wheel with a steep metal grid, a dome home, a plastic Lego-like

block, and sunflower seeds. Mice were weighed immediately before tamoxifen administration and then weighted once per week during home-cage changes for the first three weeks after tamoxifen administration. Mice were kept in the same housing conditions until the end of the protocol (18 weeks) with access to food and water *ad libitum*. Home-cages in both CE and EE were changed weekly. Enrichment material was checked every week: new tissue paper and sunflower seeds were added weekly, while cardboard tubes, dome homes, and aspen bricks were replaced when destroyed or highly degraded. The remaining enrichment material was constantly transferred to the new cage in the weekly home-cage changes. The spatial organization of the enrichment material was maintained throughout the experiment. Manipulation of mice during the behavioral test period was reduced to the minimum necessary.

Behavioral tests: Procedures were conducted in the dark phase of the light/dark cycle and performed blind to genotypes. The order and interval between tests were used as acclimation for the next test and performed in the following order: (1) three-chamber sociability; (2) novel object recognition; (3) Y-maze; (4) step-down passive avoidance. The Morris water maze test was conducted in separate and independent animal cohorts. The experimenter recording the behavioral parameters during test sections was blind to genotype.

Three-chamber sociability: Mice were first habituated to the empty apparatus, a three-chamber box consisting of three interconnected lined compartments, for 10 minutes. After the habituation phase, mice were tested in the sociability task. In this phase, subject mice socialize with a conspecific mouse in a cage or explore an empty cage in opposite external compartments. All phases during 10 minutes and the placement of stranger mice on the left or right side of the chamber are systematically altered between trials. The time spent in each compartment (four paws have entered the chamber) and the exploration time (direct contact or stretching in an area of 3 – 5 cm around the mouse or empty cage) were measured. All parameters were evaluated by Boris software (*36*). Because female control mice did not significantly enhance sociability parameters, only male mice (both genotypes) were used in this test. Statistical analyses were conducted using three-way ANOVA (exploration times in empty and stranger compartments were fixed as row factors) or randomized-block two-way ANOVA (mice were considered the experimental units; statistical significance was defined as $P < 0.01$) with sphericity assumption and the Turkey correction for multiple comparisons.

Object recognition (NOR): The NOR test used experimental procedures similar to the three-chamber test. The test consists of three phases. During the habituation phase, mice can explore the apparatus for 10 min (used to perform habituation in three-chamber test, 24 h before). The next day, during the object familiarization/acquisition phase, two identical objects were placed at the center of each outer chamber. Mice were allowed to explore the objects for 10 min freely. Then mice were returned to their home cage, and after 4 h (inter-trial interval, ITI), the retention phase was performed. In this phase, one of the familiar objects is changed by a novel object, and animals are allowed to explore these objects for 3 min. Exploration was defined as follows: the mouse touched the object with its nose, or the mouse's nose was directed toward the object at a distance shorter than 2 cm. The discrimination index (DI) was calculated as before (*4*) and used as an index of memory function, DI = (time exploring the novel object) / (total time spent exploring both objects). All parameters were evaluated by Boris software (*36*). Statistical analyses were conducted using randomized-block two-way ANOVA (mice were considered the experimental units; statistical significance was defined as $P < 0.05$) with sphericity assumption and the Turkey correction for multiple comparisons.

Y-maze: Wrong arm returns (# errors), a measure of spatial working memory, was assessed by allowing mice to explore all three arms of the maze, motivated by an innate interest of rodents to explore previously unvisited areas. The mice are positioned in the center of the apparatus and allowed to explore freely for 8 minutes. During the test, visual clues were placed on the walls. Entries in the same arm during the spontaneous alternation

phase were considered wrong arm returns and used as the number of working memory errors. Statistical analyses were conducted using randomized-block two-way ANOVA (mice were considered the experimental units; statistical significance was defined as $P < 0.05$) with sphericity assumption and the Turkey correction for multiple comparisons.

Step-down passive avoidance: The step-down test was used to assess the long-term memory and consisted of two phases. First, in the training phase, each mouse was placed in the center of an elevated platform (15 mm above the grid floor), and the step-down from the platform with four paws was immediately followed by a foot-shock (0.5 mA) for 2 s. The latency to step-down was measured (maximum of 120s; minimum 10 s). Afterward, the animals were presented to the retention phase 24 h after training. This phase was conducted in the absence of shock, and the step-down latency from the platform was recorded (up to 120 s) and evaluated as indicators of memory retention. The retention index was calculated using the step-down latency from the test session divided by the latency from the training session. Statistical analyses were conducted using three-way ANOVA (step-down latencies in training and retention were fixed as row factors) or randomized-block two-way ANOVA with sphericity assumption. The Turkey correction for multiple comparisons was conducted in both analyses. Moreover, mice were considered the experimental units, and statistical significance was defined as $P < 0.05$.

Morris water maze (MWM): The MWM was used to evaluated learning and spatial memory. The apparatus consisted of a circular pool (110 cm diameter) filled with water (21±1ºC) made opaque gray. Visual cues were positioned equidistant in the walls. Cued learning was performed during the first two days. A non-visible escape platform (7 x 8 cm) was submerged 1 cm below the water surface in the quadrant center. In this phase, mice were trained to find the hidden platform which had a visual clue. Animals were subjected to four consecutive swimming trials, which had a different start and goal position. In the acquisition phase (4 trials/day for five days), mice were given up to 60 seconds per trial to find the hidden platform and were required to remain seated on the platform for 10 s. The platform location is the same during the acquisition phase (center of target quadrant). Escape latency (i.e., time to locate the platform) was measured during the cue learning and acquisition phase. During the probe test (day 8), the platform was removed from the pool, and each mouse was given up to 30 s to search the platform's position. All parameters were automatically evaluated by SMART v3.0 software (Panlab, Barcelona, Spain). Statistical analyses to assess learning were conducted using repeated measures two-way ANOVA (mice were considered the experimental units; statistical significance was defined as $P < 0.05$) with the Greenhouse-Geisser correction (to combat sphericity violation). In the probe test, statistical analyses were conducted using unpaired t-test (mice were considered the experimental units; statistical significance was defined as $P < 0.05$).

Adeno-associated virus (AAV) injections and quantification of dendritic spines: Mice were anesthetized by isoflurane inhalation and positioned on a stereotactic frame. Mice eyes were lubricated to prevent cornea dryness. The animal was maintained with a Stoelting™ Rodent Warmer device with a rectal probe to keep its temperature at 37ºC. Deep anesthesia was confirmed by the absence of a response to a toe pinch. We used the following coordinates to target the hippocampus: anteroposterior (AP) -2.3, mediolateral (ML) ±1.3 mm, dorsoventral (DV) -2.2 mm, using the bregma as reference. Only the right hippocampus of each animal was injected with pAAV-hSyn-mCherry (Addgene viral prep # 114472-AAV5). The viral titer was 7×10^{12} vg/mL. The red fluorescent protein (mCherry) was driven by the synapsin-1 promoter.

The surgical procedure started with a skin incision in the mouse's head to expose the bregma. After the correct X: Y localization, a drill was used to puncture the skull. The needle was slowly introduced into the animal's brain until it reached the right z coordinate. We waited 2 minutes for tissue accommodation before the AAV administration. To optimize neuronal labeling to subjacent cortical areas, we injected 0.5 µl of undiluted viral preparation (corresponding to 7×10^{12} viral genomes (vg)) into the right hippocampus at a rate of 0.1 µl/min. The needle was removed 2 min after administration, the skin was sutured, and

isoflurane flow stopped. After waking up, mice were put in a new cage for the first 24 hours, with wet food in the cage bedding, paracetamol in the water bottle, and dietary supplements (anima strath and Duphalyte®) to avoid weight loss and malnutrition.

Dendritic spines were reconstructed using Imaris. Briefly, dendrites were traced with the filaments tool using the AutoPath algorithm. The dendrite diameter was rebuilt using the shortest distance from the distance map algorithm with the local contrast threshold. Spines were detected with seed points set to 0.3 µm and the maximum spine length at 3 µm. The spine diameter was rebuild using the shortest distance from the distance map algorithm with the local contrast threshold. Statistical analyses were conducted using nested t-test (to combat pseudoreplication) with spine density per dendrite stacked within each mouse (statistical significance was defined as $P < 0.05$).

Tissue preparation and immunofluorescence: After animal perfusion with ice-cold PBS (15 ml), brains were fixed by immersion in 4% PFA in phosphate buffer, pH 7.2 overnight. After that, brains were washed with PBS and then cryoprotected using a sucrose gradient in a row (15 and 30%). After 24 h, brains were mounted in an OCT embedding medium, frozen, and cryosectioned in the CM3050S Cryostat (Leica Biosystems). Coronal sections from brains (30 µm thickness) were collected non-sequentially on Superfrost ultra plus slides. Tissue sections from controls and experimental mice encompassing identical stereological regions were collected on the same glass slide and stored at -20°C. Frozen sections were defrosted for at least 1 hour and hydrated with PBS for 15 min. Sections were permeabilized with 0.25% Triton X-100 for 15 min, washed with PBS for 10 min and blocked (5% BSA, 5% FBS, 0.1% Triton X-100) for 1 hour. Primary antibodies were incubated in a blocking solution in a humidified chamber overnight at 4°C. Secondary antibodies were incubated for 2 hours in a blocking solution. After the secondary antibody, sections were washed three times for 10 min with PBS. Slides were coverslipped using glycergel or Immumount.

Confocal imaging and morphometric analysis: Images from tissue sections of the neocortex were acquired in 8-bit sequential mode using standard TCS mode at 400 Hz. The pinhole was kept at one airy in the Leica TCS SP8 confocal microscope. Images were illuminated with different laser combinations and resolved at 512 x 512 or 1024 x 1024 pixels format using HyD detectors, and entire Z-series were acquired from tissue sections. Equivalent stereological regions were obtained for all tissue sections within a given slide.

To quantify neurons (NeuN+ cells), the number of cells was manually scored, as before (*4, 37*), in stereological identical regions of the neocortex of stained sections (3 images per section; 3 sections per mice for each experimental group). Statistical analyses comparing two genotypes were conducted using the Mann-Whitney test (mice were considered the experimental units; statistical significance was defined as $P < 0.05$). Statistical analyses comparing the effect of LPS between genotypes were conducted using two-way ANOVA (tissue sections were considered the experimental units; statistical significance was defined as $P < 0.05$) with the Šidák correction for multiple comparisons.

To quantify synapses, images from stereological identical neocortical regions from each experimental group (3 images per section; 3 sections per animal for each experimental group) were acquired using a Leica HC PL APO CS 40x /1.10 CORR water objective at 1024 x 1024 pixels resolution with 8-bit bidirectional non-sequential scanner mode at 400 Hz and pinhole at one airy in the Leica TCS SP5 II confocal microscope. Z-stacks were converted to maximum projection images using the LAS AF routine. Z-projections were background-subtracted using the rolling ball background subtraction built-in algorithm in FIJI, and then images were upsampled using a bicubic interpolation routine. The number of double-positive PSD-95/vGlut1 puncta per μm^2 was manually scored for each image. Statistical analyses comparing two genotypes were conducted using the Mann-Whitney test (tissue sections (three per mice) were considered the experimental units; statistical significance was defined as $P < 0.05$).

Colocalization analyses were carried out in Imaris or FIJI using the Coloc2 plugin (https://imagej.net/Coloc_2). Statistical analyses comparing two genotypes were conducted using the Mann-Whitney test (mice or single microglia were considered the experimental units; statistical significance was defined as $P < 0.05$). Statistical analyses comparing four groups were conducted using randomized-block two-way ANOVA (single microglia were considered the experimental units; statistical significance was defined as $P < 0.05$) with sphericity assumption and the Šidák correction for multiple comparisons.

Flow cytometry and cell sorting: The following markers were used to characterize microglia in the samples: CD45 CD11b and Ly6C. Microglia were collected from the brains of control and mutant mice using density gradient separation as before (*4, 37*). Single-cell suspensions (5×10^5 cells) were incubated with different mixes of FACS antibodies for 30 min at 4°C in the dark. Compensation settings were determined using spleen from both control and mutant. Cell suspensions were evaluated on a FACS Canto II analyzer (BD Immunocytometry Systems). Cell suspensions were seeded in a U bottom 96-well plate. For GDNF staining, cells were treated with Brefeldin A (10 µg/mL) for 3 h at 37ºC in RPMI supplemented with 1% Pen/Strep and 10% FBS. Cells were incubated with CD45-PE and CD11b-Alexa Fluor 647. After antibody washing, for intracellular staining, cells were fixed in 2% PFA for 30 min, washed in PBS, and permeabilized with permeabilization buffer (Life Technologies 00-8333-56). Intracellular antibody staining mix was prepared in permeabilization buffer and incubated with the cells for 1 h at 4ºC in the dark. After washing in permeabilization buffer, cells were incubated with Alexa Fluor 488 secondary antibody for 30 min at 25ºC in the dark. After that, cells were washed twice in permeabilization buffer, resuspended in FACS staining buffer (2% BSA, 0.1% sodium azide), and analyzed in FACS Canto II. Antibody controls for Rac1 and GDNF staining (FMO) were prepared in mixes with CD45-PE and CD11b-Alexa Fluor 647 plus secondary antibodies alone. Cell sorting was performed on a FACS ARIA cell sorter as before (*4*). Data were analyzed by FlowJo X10 software (TreeStar).

Statistical analyses comparing two genotypes were conducted using the Mann-Whitney test (mice were considered the experimental units; statistical significance was defined as $P < 0.05$). Statistical analyses comparing three different genotypes were conducted using the Kruskal-Wallis test (mice were considered the experimental units; statistical significance was defined as $P < 0.05$) with the two-stage linear step-up procedure of Benjamini, Krieger, and Yekutieli correction for multiple comparisons. Statistical analyses comparing the effect of LPS between genotypes were conducted using two-way ANOVA (mice were considered the experimental units; statistical significance was defined as $P < 0.05$) with the Šidák correction for multiple comparisons.

MACS isolation of microglia: Mice (males) were perfused with ice-cold PBS, and their brains were removed. The right hemisphere was mechanically dissociated in ice-cold Dounce buffer (15mM HEPES; 0,5% Glucose; and DNAse) by six strokes in a tissue potter. Homogenate was pelleted by centrifugation, resuspended in MACS buffer (0.5% BSA; 2 mM EDTA in PBS) followed by incubation with 80 µL myelin removal microbeads. Homogenate was negatively selected using LS columns, pelleted, washed twice, resuspended in MACS buffer, and incubated 10 µL CD11b microbeads. $CD11b^+$ fraction was selected using LS columns according to the manufacture's instructions. Eluted CD11b-enriched fraction was centrifuged (9300 g; 1 min; 4ºC) and reserved for RNA isolation. RNA was isolated using the RNeasy Plus Micro Kit. RNA integrity was analyzed using the Bioanalyzer 2100 RNA Pico chips (Agilent Technologies, CA, USA).

Library preparation, Sequencing, and Bioinformatics: Ion Torrent sequencing libraries were prepared according to the AmpliSeq Library prep kit protocol as we did before (*38*). Briefly, 1 ng of highly intact total RNA was reverse transcribed. The resulting cDNA was amplified for 16 cycles by adding PCR Master Mix and the AmpliSeq mouse transcriptome gene expression primer pool. Amplicons were digested with the proprietary FuPa enzyme,

and then barcoded adapters were ligated onto the target amplicons. The library amplicons were bound to magnetic beads, and residual reaction components were washed off. Libraries were amplified, re-purified, and individually quantified using Agilent TapeStation High Sensitivity tape. Individual libraries were diluted to a 50 pM concentration and pooled equally. Emulsion PCR, templating, and 550 chip loading were performed with an Ion Chef Instrument (Thermo Scientific MA, USA). Sequencing was performed on an Ion S5XL™ sequencer (Thermo Scientific MA, USA) as we did before (*38*).

Data from the S5 XL run processed using the Ion Torrent platform-specific pipeline software Torrent Suite v5.12 to generate sequence reads, trim adapter sequences, filter and remove poor signal reads, and split the reads according to the barcode. FASTQ and BAM files were generated using the Torrent Suite plugin FileExporter v5.12. Automated data analysis was done with Torrent Suite™ Software using the Ion AmpliSeq™ RNA plugin v.5.12 and target region AmpliSeq_Mouse_Transcriptome_V1_Designed as we did before (*38*).

Raw data was loaded into Transcriptome Analysis Console (4.0 Thermo Fisher Scientific, MA, EUA) and first filtered based on ANOVA eBayes using the Limma package and displayed as fold change. Significant changes had a p-value < 0.05 and FDR < 0.2. Functional enrichment analyses were performed using Gene Set Enrichment Analysis (GSEA) with WEB-based Gene Set Analysis Toolkit (WebGestalt) (*39*), and STRING ranked enrichment (SRE) (*40*). The whole transcriptome gene list was ranked (linear fold change*-log10 FDR) and submitted to WebGestalt (http://www.webgestalt.org) or STRING (https://string-db.org/cgi/input?sessionId=bFzQ6nknJDLN&input_page_show_search=on). Pathway enrichment was performed using the REACTOME database, with default settings. Enrichment scores for gene sets were calculated using an FDR cutoff of 0.05. Enriched pathways were manually recategorized to core transcriptomic modules and are displayed as a network (constructed using Cytoscape). Contingency analyses covering different microglial phenotypes were performed using Fisher's exact test and the Baptista-Pike method to calculate the odds ratio.

Gene expression by qRT-PCR: Isolate II RNA Micro kit (Bioline) according to the manufacturer's instructions. cDNA synthesis was performed using 300 ng of total RNA (DNase I treated) with SuperScript® III First-Strand Synthesis SuperMix. qRT-PCR was carried out using iQ™ SYBR® Green Supermix on an iQ™5 multicolor real-time PCR detection system (Bio-Rad). The expression of PCR transcripts was calculated using the $2^{-deltaCt}$ with *Yhwaz* serving as the internal control gene. Statistical analyses were performed on raw $2^{-deltaCt}$ values to detect differentially expressed transcripts between sampled groups. Statistical analyses were conducted using Mann-Whitney (mice were considered the experimental units; statistical significance was defined as $P < 0.05$).

Synaptosomal preparations, high-throughput proteomics data acquisition, and quantification: Synaptosomes were acutely prepared as before (*37*). One hundred micrograms of synaptosomal proteins from each sample were processed for proteomic analysis following the solid-phase-enhanced sample-preparation (SP3) protocol. Enzymatic digestion was performed with trypsin/LysC (2 micrograms) overnight at 37◦C at 1000 rpm. The resulting peptide concentration was measured by fluorescence. Enrichment for phosphorylated peptides was performed using Titanium dioxide beads (TiO2; ThermoFisher Scientific) as described in the manufacturer's protocol.

Protein identification and quantitation were performed by nanoLC-MS/MS using an Ultimate 3000 liquid chromatography system coupled to a Q-Exactive Hybrid Quadrupole-Orbitrap mass spectrometer (Thermo Scientific, Bremen, Germany). Five hundred nanograms of peptides of each sample were loaded onto a trapping cartridge (Acclaim PepMap C18 100 Å, 5 mm × 300 µm i.d., 160454, Thermo Scientific, Bremen, Germany) in a mobile phase of 2% ACN, 0.1% FA at 10 µL/min. After 3 min loading, the trap column was switched in-line to a 50 cm × 75 µm inner diameter EASY-Spray column (ES803, PepMap RSLC, C18, 2 µm, Thermo Scientific, Bremen, Germany) at 300 nL/min. Separation was

achieved by mixing A: 0.1% FA and B: 80% ACN, 0.1% FA with the following gradient: 5 min (2.5% B to 10% B), 120 min (10% B to 30% B), 20 min (30% B to 50% B), 5 min (50% B to 99% B), and 10 min (hold 99% B). Subsequently, the column was equilibrated with 2.5% B for 17 min. Data acquisition was controlled by Xcalibur 4.0 and Tune 2.9 software (Thermo Scientific, Bremen, Germany).

The mass spectrometer was operated in the data-dependent (dd) positive acquisition mode alternating between a full scan (*m*/*z* 380-1580) and subsequent HCD MS/MS of the 10 most intense peaks from a full scan (normalized collision energy of 27%). The ESI spray voltage was 1.9 kV. The global settings were as follows: use lock masses best (*m*/*z* 445.12003), lock mass injection Full MS and chrom. peak width (FWHM) of 15 s. The full scan settings were as follows: 70 k resolution (*m*/*z* 200), AGC target 3×10^6, maximum injection time 120 ms; dd settings: minimum AGC target 8×10^3, intensity threshold 7.3×10^4, charge exclusion: unassigned, 1, 8, >8, peptide match preferred, exclude isotopes on, and dynamic exclusion 45 s. The MS2 settings were as follows: microscans 1, resolution 35 k (*m*/*z* 200), AGC target 2×10^5, maximum injection time 110 ms, isolation window 2.0 *m*/*z*, isolation offset 0.0 *m*/*z*, dynamic first mass, and spectrum data type profile.

The raw data were processed using the Proteome Discoverer 2.5.0.400 software (Thermo Scientific, Bremen, Germany). Protein identification analysis was performed with the data available in the UniProt protein sequence database for the *Mus Musculus* Proteome (2020_02 version, 55,398 entries) and a common contaminant database from MaxQuant (version 1.6.2.6, Max Planck Institute of Biochemistry, Munich, Germany). Sequest HT tandem mass spectrometry peptide database search program was used as the protein search algorithm. The search node considered an ion mass tolerance of 10 ppm for precursor ions and 0.02 Da for fragment ions. The maximum allowed missing cleavage sites was set as 2. For the phosphoproteomics, the IMP-ptmRS node, with the PhosphoRS mode (set to false), was used to localize phosphorylation sites. The Inferys rescoring node was considered, and the processing node Percolator was enabled with the following settings: maximum delta Cn 0.05; decoy database search target False Discovery Rate—FDR 1%; validation based on q-value. Protein-label-free quantitation was performed with the Minora feature detector node at the processing step. Precursor ion quantification used the processing step with the following parameters: Peptides: unique plus razor; precursor abundance was based on intensity; normalization mode was based on the total peptide amount; the pairwise protein ratio calculation and hypothesis test were based on a *t*-test (background based). The Feature Mapper node from the Proteome Discoverer software was used to create features from unique peptide-specific peaks within a short retention time and mass range. This was achieved by applying a chromatographic retention time alignment with a maximum shift of 10 min and 10 ppm of mass tolerance allowed for mapping features from different sample files. For feature linking and mapping, the minimum signal to noise (S/N) threshold was set at 5.

For the determination of DE between groups, the following filters were used: (1) only master proteins detected with high/medium confidence FDR; (2) a protein/phosphoprotein must be detected in more than 50% of samples in each experimental group (except for proteins that were depleted entirely in one of the experimental groups); (3) the *p*-value adjusted using Benjamini–Hochberg correction for the FDR was set to ≤ 0.05; (4) at least 50% of samples with protein-related peptides sequenced by MS/MS; (5) the peptide spectrum matches (PSMs) was set to ≥ 2.

Proteome bioinformatic analyses: For constructing similarity matrices, DE proteins retrieved from the LFQ experience were uploaded to SynGO (a systematic knowledgebase of functionally-annotated synaptic genes based exclusively on published experimental data (https://syngoportal.org (*41*))) to map $Rac1^{fl/fl}$ and $Cx3cr1^{CreER+}$:$Rac1^{fl/fl}$ synaptosomes (proteins and GO terms). A one graph-based (*42*) pairwise semantic similarity based on the topology of the GO graph structure (Cellular Component ontology) was computed using GoSemSim (*43*) in the R package within Bioconductor (*44*). The same package was used to calculate the semantic similarity among protein clusters using the Best-Match Average

(BMA) strategy, aggregating various semantic similarity scores of multiple associated GO terms. Agglomerative Hierarchical clustering using the Ward Linkage was also performed for the similarity matrices.

For network integration and synaptic topographic maps, the set of DE synaptosomal proteins and phosphoproteins were first inputted in SynGO. The DE proteins/phosphoproteins were flagged to presynaptic or postsynaptic compartments using SynGO cellular components' anthology (dataset release version 20210225). DE proteins of the proteomic dataset positively mapped to SynGO were subsequently screened for synaptic interactors/partners using protein-binding interfaces via inter-protein cross-links in the Stitch database (https://xlink.cncr.nl (*45*)). DE phosphoproteins of the phosphoproteomic dataset were inspected and cross-checked using the comprehensive web portal PhosphositePlus (https://www.phosphosite.org/homeAction.action (*46*)). Putative protein kinases controlling the phosphorylation of the filtered phosphopeptides were identified using NetworKIN 3.0 (http://networkin.info/index.shtml (*47*)). DE phosphoproteins were then screened for synaptic interactors/partners using Stitch and Mechismo (*48*). Pathway enrichment analyses (FDR cutoff < 0.05 with the Benjamini-Hochberg multiple test adjustments) were carried out in WebGestalt (*39*) with REACTOME and GO as functional databases. Network construction and clustering were carried out using k-means clustering in STRING (*40*) and Omics Visualizer (*49*) in Cytoscape.

Microglial cell line, live-cell imaging, and FRET: The human microglial cell line HMC3 was obtained from ATCC (ATCC® CRL-3304™). Cells were cultivated and maintained as before (*4, 37, 50*). HMC3 microglia were plated on plastic-bottom culture dishes (µ-Dish 35 mm, iBidi) and transfected, as before (*50*), with different biosensors.

Imaging was performed using a Leica DMI6000B inverted microscope. The excitation light source was a mercury metal halide bulb integrated with an EL6000 light attenuator. High-speed, low vibration external filter wheels (equipped with CFP/YFP/farRed excitation and emission filters) were mounted on the microscope (Fast Filter Wheels, Leica Microsystems). A 440-520nm dichroic mirror (CG1, Leica Microsystems) and a PlanApo 63X 1.3NA glycerol immersion objective were used for CFP and FRET images. Images were acquired with 2 x 2 binning using a digital CMOS camera (ORCA-Flash4.0 V2, Hamamatsu Photonics). Quantifications were performed in FIJI, as before (*50*), using the precision FRET (PFRET) data processing software package for ImageJ (https://lvg.virginia.edu/digital-downloads/pfret-data-processing-software). The mean gray intensity values from ratio images were normalized using the deltaF/F0 for statistics. Representative images are shown in intensity-modulated display (*50*). Statistical analyses were conducted using repeated measures two-way ANOVA (individual microglial cells were considered the experimental units; statistical significance was defined as $P < 0.05$) with the Greenhouse-Geisser correction (to combat sphericity violation) and the Šidák correction for multiple comparisons.

Immunofluorescence quantification on cultured microglia: HMC3 microglia were cultivated in glass coverslips and transfected, as before (*50*). Coverslips were fixed with 4% PFA and immunolabeling was performed as before (*4, 37, 51*). Then, coverslips were mounted with Immumount and visualized in a Leica DMI6000B inverted epifluorescence microscope using a PlanApo 63X/1.3NA glycerol immersion objective. Images were acquired using a digital CMOS camera (ORCA-Flash4.0 V2, Hamamatsu Photonics).

Quantification of Rac1 and Rab27a fluorescence was carried out as before (*4, 37, 51*). GDNF quantifications were performed using the precision FRET (PFRET) data processing software package for ImageJ (https://lvg.virginia.edu/digital-downloads/pfret-data-processing-software). The native 32-bit values from ratio images (GDNF over mCherry or YFP) were used for statistics. Ratio images are shown in intensity-modulated display (*50*). Statistical analyses were conducted using unpaired t-test (single cells were considered the experimental units; statistical significance was defined as $P < 0.05$).

Primary microglial cultures and collection of microglia conditioned media (MCM): Primary cultures of cortical microglia from neonatal Wistar rats were prepared as before (*38, 51*). Cultures were infected with lentiviruses carrying pLKO-empty or pLKO-Rac1 shRNA as before (*4, 37, 51*). Replication-incompetent lentiviral particles were prepared as before (*4, 51, 52*). After viral removal and medium refeed, microglia were cultured for 5 days. Then, the culture medium (MCM) was collected, centrifuged for debris removal (1200 rpm, 5 min), and frozen at −80 °C until used.

Primary cultures of cortical neurons and single-spine live imaging: Brain cortices were dissected from embryonic day 18 Wistar rat embryos and dissociated using trypsin (0.25%, v/v). Neurons were plated at a final density of 1×10^4 to 5×10^4 cells per dish and cultured in the presence of a glial feeder layer. Cells were cultured in phenol red-free Neurobasal medium supplemented with B27 supplement (1:50, v/v), 25 mM glutamate, 0.5 mM glutamine, and gentamicin (0.12 mg/ml). To prevent glial overgrowth, neuronal cultures were treated with 5 mM cytosine arabinoside after 3 days in vitro and maintained in a humidified incubator with 5% CO_2/95% air at 37°C for up to 2 weeks, feeding the cells once per week by replacing one-third of the medium. Cortical neurons were plated on plastic-bottom culture dishes (µ-Dish 35 mm, iBidi) and co-transfected using the calcium phosphate method, as before (*4, 37, 51*), with mCherry-Lifeact-7 and pGP-CMV-GCaMP6f. Experiments were carried out by recording neuronal cultures with microglia conditioned media (MCM) for 10 minutes (baseline) and then in the presence of MCM + KCl 20 mM (neuronal stimulation).

Imaging was performed using a Leica DMI6000B inverted microscope. The excitation light source was a mercury metal halide bulb integrated with an EL6000 light attenuator. The L5 (Ex: 460-500; BS: 505; Em: 512-542) and TX2 (Ex: 540-580; BS: 595; Em: 607-683) filter set and a PlanApo 63X 1.3NA glycerol immersion objective were used. Images were acquired with 2 x 2 binning using a digital CMOS camera (ORCA-Flash4.0 V2, Hamamatsu Photonics). Quantification of spine area was performed in FIJI, as before (*50*). The mean gray intensity values from spine GCaMP6f and spine actin dynamics (lifeact fluorescence signal) were normalized using the $\Delta F/F$. Representative GCaMP6f images are shown in intensity-modulated display (*50*).

Data for activity-dependent spine remodeling/calcium dynamics over time were fit using a beta growth and decline model (Y=Ym*(1+ (Te - X)/(Te - Tm))*(X/Te)^(Te/(Te-Tm))) for spine expansion and a plateau followed by one-phase exponential decay (Y= IF(X<X0, Y0, Plateau+(Y0-Plateau)*exp(-K*(X-X0)))) for spine retraction. Spines that collapsed or were eliminated during the evoked neuronal activity were excluded from the analysis. The further additional filters were used for data exclusion: spine expansion < 2.5% spine area; spine retraction < 2% spine area; calcium signal < 25% amplitude increase. Linear regression (with the % spine area as the Y variable) was used to predict how changes in activity-dependent calcium and actin dynamics contributed to spine remodeling. Statistical analyses were conducted using unpaired t-test with single spines measurements as the experimental units (statistical significance was defined as $P < 0.05$). ANCOVA was used to compare slopes inferred from linear regression analyses.

Statistics: Experimenters were blinded to genotypes, and whenever possible, housing conditions. Statistical tests and their respective significance thresholds are detailed in each subsection of the Experimental Procedures (see above). Descriptive statistics for each dataset are defined in Figure Legends. Statistical analysis and graph construction were performed in GraphPad Prism version 9.0.2 for macOS. Finalized figures were assembled in Adobe Illustrator 2020 (version 24.3).

Acknowledgments

Work in the JBR laboratory was financed by FEDER—Fundo Europeu de Desenvolvimento Regional funds through the COMPETE 2020—Operational Programme for Competitiveness and Internationalisation (POCI), Portugal 2020, and by Portuguese funds through FCT—Fundação para a Ciência e a Tecnologia/Ministério da Ciência, Tecnologia e Ensino Superior in the framework of the project POCI-01-0145-FEDER-031318 (PTDC/MED-NEU/31318/2017).

Work in the TS laboratory was financed by FEDER—Fundo Europeu de Desenvolvimento Regional funds through the COMPETE 2020—Operational Programme for Competitiveness and Internationalisation (POCI), Portugal 2020, and by Portuguese funds through FCT—Fundac□ão para a Cie□ncia e a Tecnologia/Ministério da Cie□ncia, Tecnologia e Ensino Superior in the framework of the project POCI-01-0145-FEDER-030647 (PTDC/ SAU-TOX/30647/2017).

IMP acknowledges funding from European Union's Seventh Framework Programme for research, technological development and demonstration (Marie Curie Actions) under grant agreement no 600375.

CCP and RS hold employment contracts financed by national funds through FCT—in the context of the program-contract described in paragraphs 4, 5, and 6 of art. 23 of Law no. 57/ 2016, of August 29, as amended by Law no. 57/2017 of July 2019. TC, TOA, JTM, and AM were supported by FCT (SFRH/BD/117148/2016, SFRH/BD/147981/2019, Fellow/PhD_Programs_i3S/1102/2021, IF/00753/2014).

The authors acknowledge the support of the following i3S Scientific Platforms: Advanced Light Microscopy (ALM), a member of the national infrastructure PPBI-Portuguese Platform of BioImaging; Animal Facility; Cell culture and Genotyping; Genomics; Proteomics; and Translational Cytometry. We thank João Morais-Cabral for critically discussing the manuscript.

References

1. T. R. Hammond, D. Robinton, B. Stevens, Microglia and the Brain: Complementary Partners in Development and Disease. *Annu Rev Cell Dev Biol* **34**, 523-544 (2018).
2. P. T. Nguyen *et al.*, Microglial Remodeling of the Extracellular Matrix Promotes Synapse Plasticity. *Cell* **182**, 388-403.e315 (2020).
3. C. N. Parkhurst *et al.*, Microglia promote learning-dependent synapse formation through brain-derived neurotrophic factor. *Cell* **155**, 1596-1609 (2013).
4. R. Socodato *et al.*, Microglia Dysfunction Caused by the Loss of Rhoa Disrupts Neuronal Physiology and Leads to Neurodegeneration. *Cell Rep* **31**, 107796 (2020).
5. A. Ndoja *et al.*, Ubiquitin Ligase COP1 Suppresses Neuroinflammation by Degrading c/EBPβ in Microglia. *Cell* **182**, 1156-1169.e1112 (2020).
6. C. Cserép, B. Pósfai, Á. Dénes, Shaping Neuronal Fate: Functional Heterogeneity of Direct Microglia-Neuron Interactions. *Neuron* **109**, 222-240 (2021).
7. M. Mayford, S. A. Siegelbaum, E. R. Kandel, Synapses and memory storage. *Cold Spring Harb Perspect Biol* **4**, (2012).
8. C. Kaur, Effects of colchicine on amoeboid microglial cells in the postnatal rat brain. *Archives of histology and cytology* **60**, 453-462 (1997).
9. T. Goldmann *et al.*, A new type of microglia gene targeting shows TAK1 to be pivotal in CNS autoimmune inflammation. *Nat Neurosci* **16**, 1618-1626 (2013).
10. S. Yona *et al.*, Fate mapping reveals origins and dynamics of monocytes and tissue macrophages under homeostasis. *Immunity* **38**, 79-91 (2013).
11. A. Chrostek *et al.*, Rac1 is crucial for hair follicle integrity but is not essential for maintenance of the epidermis. *Mol Cell Biol* **26**, 6957-6970 (2006).
12. O. Butovsky *et al.*, Identification of a unique TGF-β-dependent molecular and functional signature in microglia. *Nat Neurosci* **17**, 131-143 (2014).
13. C. Sousa *et al.*, Single-cell transcriptomics reveals distinct inflammation-induced microglia signatures. *EMBO Rep* **19**, (2018).
14. A. S. Mendiola *et al.*, Transcriptional profiling and therapeutic targeting of oxidative stress in neuroinflammation. *Nat Immunol* **21**, 513-524 (2020).
15. H. Keren-Shaul *et al.*, A Unique Microglia Type Associated with Restricting Development of Alzheimer's Disease. *Cell* **169**, 1276-1290.e1217 (2017).
16. T. R. Hammond *et al.*, Single-Cell RNA Sequencing of Microglia throughout the Mouse Lifespan and in the Injured Brain Reveals Complex Cell-State Changes. *Immunity* **50**, 253-271.e256 (2019).
17. G. Paratcha, F. Ledda, C. F. Ibáñez, The neural cell adhesion molecule NCAM is an alternative signaling receptor for GDNF family ligands. *Cell* **113**, 867-879 (2003).
18. U. Drescher, Axon Guidance: Push and Pull with Ephrins and GDNF. *Current Biology* **21**, R30-R32 (2011).
19. F. Ledda, G. Paratcha, T. Sandoval-Guzmán, C. F. Ibáñez, GDNF and GFRalpha1 promote formation of neuronal synapses by ligand-induced cell adhesion. *Nat Neurosci* **10**, 293-300 (2007).
20. D. Irala *et al.*, The GDNF-GFRα1 complex promotes the development of hippocampal dendritic arbors and spines via NCAM. *Development* **143**, 4224-4235 (2016).
21. A. Bonafina *et al.*, GDNF and GFRα1 Are Required for Proper Integration of Adult-Born Hippocampal Neurons. *Cell Rep* **29**, 4308-4319.e4304 (2019).
22. L. Lonka-Nevalaita *et al.*, Characterization of the intracellular localization, processing, and secretion of two glial cell line-derived neurotrophic factor splice isoforms. *J Neurosci* **30**, 11403-11413 (2010).
23. J. B. Pereira-Leal, M. C. Seabra, Evolution of the rab family of small GTP-binding proteins11Edited by J. Thornton. *Journal of Molecular Biology* **313**, 889-901 (2001).
24. M. Matsuzaki, N. Honkura, G. C. R. Ellis-Davies, H. Kasai, Structural basis of long-term potentiation in single dendritic spines. *Nature* **429**, 761-766 (2004).

25. M. Fu, Y. Zuo, Experience-dependent structural plasticity in the cortex. *Trends in Neurosciences* **34**, 177-187 (2011).
26. K. M. Woolfrey, M. L. Dell'Acqua, Coordination of Protein Phosphorylation and Dephosphorylation in Synaptic Plasticity. *J Biol Chem* **290**, 28604-28612 (2015).
27. J. A. Bibb, M. R. Mayford, J. Z. Tsien, C. M. Alberini, Cognition Enhancement Strategies. *The Journal of Neuroscience* **30**, 14987 (2010).
28. S. O. Ögren, O. Stiedl, in *Encyclopedia of Psychopharmacology,* I. P. Stolerman, Ed. (Springer Berlin Heidelberg, Berlin, Heidelberg, 2010), pp. 960-967.
29. L. M. Au - Lueptow, Novel Object Recognition Test for the Investigation of Learning and Memory in Mice. *JoVE*, e55718 (2017).
30. A. K. Kraeuter, P. C. Guest, Z. Sarnyai, The Y-Maze for Assessment of Spatial Working and Reference Memory in Mice. *Methods Mol Biol* **1916**, 105-111 (2019).
31. O. Kaidanovich-Beilin, T. Lipina, I. Vukobradovic, J. Roder, J. R. Woodgett, Assessment of social interaction behaviors. *J Vis Exp*, (2011).
32. S. Hong, B. Stevens, Microglia: Phagocytosing to Clear, Sculpt, and Eliminate. *Developmental Cell* **38**, 126-128 (2016).
33. V. Sytnyk , I. Leshchyns'ka , A. G. Nikonenko , M. Schachner NCAM promotes assembly and activity-dependent remodeling of the postsynaptic signaling complex. *Journal of Cell Biology* **174**, 1071-1085 (2006).
34. I. J. Cajigas *et al.*, The local transcriptome in the synaptic neuropil revealed by deep sequencing and high-resolution imaging. *Neuron* **74**, 453-466 (2012).
35. C. Gubert, A. J. Hannan, Environmental enrichment as an experience-dependent modulator of social plasticity and cognition. *Brain Research* **1717**, 1-14 (2019).
36. O. Friard, M. Gamba, BORIS: a free, versatile open-source event-logging software for video/audio coding and live observations. *Methods in Ecology and Evolution* **7**, 1325-1330 (2016).
37. R. Socodato *et al.*, Daily alcohol intake triggers aberrant synaptic pruning leading to synapse loss and anxiety-like behavior. *Sci Signal* **13**, (2020).
38. T. Canedo *et al.*, Astrocyte-derived TNF and glutamate critically modulate microglia activation by methamphetamine. *Neuropsychopharmacology*, (2021).
39. Y. Liao, J. Wang, E. J. Jaehnig, Z. Shi, B. Zhang, WebGestalt 2019: gene set analysis toolkit with revamped UIs and APIs. *Nucleic Acids Research* **47**, W199-W205 (2019).
40. D. Szklarczyk *et al.*, STRING v11: protein-protein association networks with increased coverage, supporting functional discovery in genome-wide experimental datasets. *Nucleic acids research* **47**, D607-D613 (2019).
41. F. Koopmans *et al.*, SynGO: An Evidence-Based, Expert-Curated Knowledge Base for the Synapse. *Neuron* **103**, 217-234.e214 (2019).
42. J. Z. Wang, Z. Du, R. Payattakool, P. S. Yu, C. F. Chen, A new method to measure the semantic similarity of GO terms. *Bioinformatics* **23**, 1274-1281 (2007).
43. G. Yu *et al.*, GOSemSim: an R package for measuring semantic similarity among GO terms and gene products. *Bioinformatics* **26**, 976-978 (2010).
44. R. C. Gentleman *et al.*, Bioconductor: open software development for computational biology and bioinformatics. *Genome Biol* **5**, R80 (2004).
45. M. A. Gonzalez-Lozano *et al.*, Stitching the synapse: Cross-linking mass spectrometry into resolving synaptic protein interactions. *Science Advances* **6**, eaax5783 (2020).
46. P. V. Hornbeck *et al.*, PhosphoSitePlus, 2014: mutations, PTMs and recalibrations. *Nucleic Acids Res* **43**, D512-520 (2015).
47. H. Horn *et al.*, KinomeXplorer: an integrated platform for kinome biology studies. *Nature Methods* **11**, 603-604 (2014).
48. M. J. Betts *et al.*, Mechismo: predicting the mechanistic impact of mutations and modifications on molecular interactions. *Nucleic Acids Res* **43**, e10 (2015).

49. M. Legeay, N. T. Doncheva, J. H. Morris, L. J. Jensen, Visualize omics data on networks with Omics Visualizer, a Cytoscape App. *F1000Res* **9**, 157 (2020).
50. R. Socodato, P. Melo, J. P. Ferraz-Nogueira, C. C. Portugal, J. B. Relvas, A Protocol for FRET-Based Live-Cell Imaging in Microglia. *STAR Protoc* **1**, 100147 (2020).
51. C. C. Portugal *et al.*, Caveolin-1-mediated internalization of the vitamin C transporter SVCT2 in microglia triggers an inflammatory phenotype. *Sci Signal* **10**, (2017).
52. C. Karabiyik *et al.*, Neuronal Rho GTPase Rac1 elimination confers neuroprotection in a mouse model of permanent ischemic stroke. *Brain Pathol* **28**, 569-580 (2018).

Figure Legends

Figure 1. A microglia-synapse nexus at the molecular level.
A, Flow cytometry analysis of Rac1 expression in microglia from Cx3cr1^{CreER+}, Rac1$^{fl/fl}$, and Cx3cr1^{CreER+}:Rac1$^{fl/fl}$ mice (n=4-5 animals per genotype). Violin plots (median and quartiles) depict Rac1 expression in microglia. ***P<0.001 (One-way ANOVA). **B and C,** Imaris rendering of dendritic spines and histological confocal colocalization of PSD-95 and vGlut1 on tissue sections from neocortices of Rac1$^{fl/fl}$ and Cx3cr1^{CreER+}:Rac1$^{fl/fl}$ mice (n=9 dendrites stacked across 3 animals per genotype (B) or n=12 slices pooled across 4 animals per genotype (C)). Violin plots (median and quartiles) depict spine density (B) or PSD-95/vGlut1 double-positive puncta (C). *P<0.05 (nested t-test (B); Mann-Whitney test (C)). Scale bars: B: 2 µm; C: 5 µm. **D and E,** Performance of Rac1$^{fl/fl}$ and Cx3cr1^{CreER+}:Rac1$^{fl/fl}$ mice in the Morris Water Maze (n=11 mice per genotype). Histogram (mean and SEM) shows the learning curves, and violin plots (median and quartiles) depict the probe tests. *p<0.05 (two-way ANOVA (D); unpaired t-test (E)). **F,** Workflow of proteomic and phosphoproteomic profiling in brain synaptosomes and dataset integration. **G and H,** Hierarchical clustering and similarity matrix heatmap of differentially expressed synaptic protein products (G) or enriched cellular component GO terms (H) from Rac1$^{fl/fl}$ and Cx3cr1^{CreER+}:Rac1$^{fl/fl}$ synaptosomes. Scales: Low (0) to high (1) similarly score colored from light blue to light coral. **I,** Pre and postsynaptic functional modules controlled by microglial Rac1 signaling revealed by proteomic and phosphoproteomic integration (n=4-5 mice per genotype). Nodes are scaled according to enrichment scores. **J-M,** Primary cortical neuronal cultures co-expressing GCamp6f and Lifeact-DsRed were recorded in saline for 10 min and then recorded upon stimulation with conditioned media from primary microglial cultures (MCM) carrying scrambled sequence or Rac1 shRNA. In all conditions, neurons were co-stimulated with 20 mM KCl. Violin plots (median and quartiles) show single-spine time-lapse fluorescence changes (n=88-112 spines pooled across 3 independent neuronal cultures). *p<0.05; ****p<0.0001 (Mann-Whitney test).

Figure 2. Microglia-synapse nexus modulates experience-dependent learning, memory, and sociability.
A, Housing conditions to elicit experience-dependent synaptic remodeling. **B,** Workflow of phosphoproteomic profiling in hippocampal synaptosomes after experience-dependent plasticity. **C,** Venn diagram allocating DE phosphoproteins across housing conditions and genotypes. **D and E,** Segregation of synaptic pathways (D) and Camk2-associated phospho-PPI hubs (E) modulated concomitantly by experience and microglia (n=3-5 mice per group). Histogram displays selected enriched pathways (D). Hubs with selected phosphoproteins related to synaptic functions are shown (E). **F,** Schematics for assessing enhancement of cognitive performance driven by experience. **G-N,** Evaluation of Rac1$^{fl/fl}$ and Cx3cr1^{CreER+}:Rac1$^{fl/fl}$ mice (n=13-16 mice (G-L) or 7-11 mice (M and N) per genotype) in the step-down passive avoidance, novel object recognition, Y-maze, and three-chamber social interaction tests. Histogram and violin plots display medians with quartiles. *p<0.05 (Three-way ANOVA (B); Two-way ANOVA (C-G); **p<0.01 and ***p<0.001 (Three-Way ANOVA).

Supplementary Figure Legends

Suppl. Figure 1. Microglial Rac1 transcriptomic signature.
A, Strategy for conditionally ablating Rac1 in brain microglia. **B,** Gating strategy for microglial isolation by flow cytometry. **C,** Rac1 mRNA amounts evaluated by qRT-PCR in microglia sorted from the brains of $Rac1^{fl/fl}$ and $Cx3cr1^{CreER+}$:$Rac1^{fl/fl}$ mice (n=3 mice per genotype). Violin plots display medians with quartiles. *p<0.05 (Mann-Whitney test). **D,** Workflow of microglial isolation, sequencing, and downstream bioinformatics analysis. **E and F,** Rac1-dependent microglia transcriptomic programs revealed by analogy concatenation of GSEA and SRA (n=3 mice per genotype). The interaction networks display the top enriched pathways within each functional module.

Suppl. Figure 2. Microglial Rac1 RNA-seq relation with known microglial transcriptomic modules.
A, Venn diagrams with contingency analyses between the differentially expressed transcripts (RNA-seq) in $Cx3cr1^{CreER+}$:$Rac1^{fl/fl}$ vs. $Rac1^{fl/fl}$ and published microglial functional transcriptomic modules. **B,** mRNA amounts evaluated by qRT-PCR in microglia (sorted as in Suppl. Fig. 1B) from the brains of $Rac1^{fl/fl}$ and $Cx3cr1^{CreER+}$:$Rac1^{fl/fl}$ mice (n=5-6 mice per genotype). Violin plots display medians with quartiles. *p<0.05; **p<0.01; ***p<0.001 (Mann-Whitney test).

Suppl. Figure 3. Rac1 is a relay switch for microglial sensing of external cues.
A, Control (scrambled) or Rac1 knocked down (KD) HMC3 microglia expressing a ROS FRET biosensor were recorded in saline before (t=0 min; baseline) and after treatment with 100 ng/ml LPS. Violin plots (median and quartiles) show time-lapse Donor/FRET ratio changes (n=16-17 cells pooled across 3 different experiments). Pseudocolor ramps display representative ratio values. *p<0.05; ****p<0.0001 (Two-Way ANOVA). Scale bar: 10 µm. **B**, Control (scrambled) or Rac1 knocked down (KD) HMC3 microglia expressing an NFkB inhibitor biosensor were recorded in saline before (t=0 min; baseline) and after treatment with 100 ng/ml LPS. Violin plots (median and quartiles) show time-lapse fluorescence changes (n=25-31 cells pooled across 3 different experiments). Pseudocolor ramps display representative fluorescence values. **p<0.01; ****p<0.0001 (Two-Way ANOVA). Scale bar: 5 µm. **C**, Control (scrambled) or Rac1 knocked down (KD) HMC3 microglia expressing a diacylglycerol (DAG) FRET biosensor were recorded in saline before (t=0 min; baseline) and after treatment with 10 ng/ml phosphatidylcholine (PC). Violin plots (median and quartiles) show time-lapse FRET/Donor ratio changes (n=50-58 cells pooled across 3 different experiments). Pseudocolor ramps display representative ratio values. **p<0.01; ***p<0.001 (Two-Way ANOVA). Scale bar: 5 µm. **D**, Control (scrambled) or Rac1 knocked down (KD) HMC3 microglia expressing an endoplasmic reticulum (ER) Ca2+ FRET biosensor were recorded in saline before (t=0 min; baseline) and after treatment with 10 ng/ml PC. Violin plots (median and quartiles) show time-lapse FRET/Donor ratio changes (n=26-42 cells pooled across 3 different experiments). Pseudocolor ramps display representative ratio values. ***p<0.001; ****p<0.0001 (Two-Way ANOVA). Scale bar: 5 µm. **E**, Control ($Rac1^{WT}$) or Rac1 dominant-negative ($Rac1^{T17N}$) HMC3 microglia expressing a cytosolic Ca2+ biosensor were recorded in saline before (t=0 min; baseline) and after treatment with 100µM ATP. Violin plots (median and quartiles) show time-lapse fluorescence changes (n=11 cells per group pooled across 3 different experiments). Pseudocolor ramps display representative fluorescence values. *p<0.05; ***p<0.001 (Two-Way ANOVA). Scale bar: 20 µm. **F**, Control ($Rac1^{WT}$) or Rac1 dominant-negative ($Rac1^{T17N}$) HMC3 microglia expressing a PKC FRET biosensor were recorded in saline before (t=0 min; baseline) and after treatment with 100µM ATP. Violin plots (median and quartiles) show FRET/Donor ratio changes (n=10 cells per group pooled across 3 different experiments). Pseudocolor ramps display representative ratio values. *p<0.05; ****p<0.0001 (Two-Way ANOVA). Scale bar: 20 µm. **G**, Histological confocal analysis of Iba1 on tissue sections from neocortices of $Rac1^{fl/fl}$ and $Cx3cr1^{CreER+}$:$Rac1^{fl/fl}$ mice after treatment with saline (CT) or intraperitoneal injection of 4

µg/kg LPS (inflammation) for 24 h (n=3 slices from 4 animals per group). Violin plots (median and quartiles) depict Iba1^{+} cell counts. *P<0.05 (Two-way ANOVA). Scale bar: 50 µm. **H**, Flow cytometry analysis of microglia from the brains of Rac1$^{fl/fl}$ and Cx3cr1^{CreER+}:Rac1$^{fl/fl}$ mice after treatment with saline (CT) or intraperitoneal injection of 4 µg/kg LPS (inflammation) for 24 h (n=8-11 animals per group). Violin plots (median and quartiles) depict microglial cell numbers. *P<0.05 (Two-way ANOVA). **I**, Histological confocal analysis of CD68 and Iba1 on tissue sections from neocortices of Rac1$^{fl/fl}$ and Cx3cr1^{CreER+}:Rac1$^{fl/fl}$ mice after treatment with saline (CT) or intraperitoneal injection of 4 µg/kg LPS (inflammation) for 24 h (n=108 cells pooled across 4 animals per group). Violin plots (median and quartiles) depict CD68 fluorescence per Iba1^{+} cell. ****p<0.0001 (Two-way ANOVA). Scale bar: 20 µm.

Suppl. Figure 4. Rac1 controls a Rab27a/GDNF signaling axis in microglia.
A, F and H, Imaris rendering of confocal images from neocortical tissue sections of Rac1$^{fl/fl}$ and Cx3cr1^{CreER+}:Rac1$^{fl/fl}$ mice (3 animals per genotype). Scale bars: 10 µm. **B, D, E, G, I, and J,** Immunofluorescence of Rac1, GDNF, or Rab27a in HMC3 microglia expressing different plasmids (scrambled-mCherry, pLKO-empty, Rac1-shRNA_mCherry, pLKO-Rab27a shRNA, FKBP-YFP+FRBLyn, or Rac1 YF+FRBLyn). Violin plots display medians with quartiles (n=36-58 cells pooled across 3 different cultures). Pseudocolor ramps display representative fluorescence ratio values. **p<0.01; ****p<0.0001 (Mann-Whitney test). Scale bars: 20 µm (B); 10 µm (D, E, G, I, and J). **C**, Flow cytometry analysis of GDNF expression in microglia from Rac1$^{fl/fl}$ and Cx3cr1^{CreER+}:Rac1$^{fl/fl}$ mice (n=5 animals per genotype). Violin plots (median and quartiles) depict GDNF^{+} microglia. *P<0.05 (Mann-Whitney test).

Suppl. Figure 5. Impact of microglial Rac1 ablation on neuronal numbers, synaptic pruning, and neuroinflammation.
A and B, Histological confocal analysis of NeuN or Iba1/CD68/PSD-95 on tissue sections from neocortices of Rac1$^{fl/fl}$ and Cx3cr1^{CreER+}:Rac1$^{fl/fl}$ mice (n= 3 slices from 4 animals per genotype (A) or n=24 cells from 4 different mice per genotype (B)). **C,** mRNA amounts evaluated by qRT-PCR in neocortices of Rac1$^{fl/fl}$ and Cx3cr1^{CreER+}:Rac1$^{fl/fl}$ mice (n=5-6 mice per genotype). Violin plots display medians with quartiles. Scale bars: A: 50 µm; B: 10 µm.

Suppl. Figure 6. Synaptic PPI network controlled by microglial Rac1.
Pre and postsynaptic PPI clusters relative to Cx3cr1^{CreER+}:Rac1$^{fl/fl}$ vs. Rac1$^{fl/fl}$ mice. Each network cluster displays selected protein nodes (integration of proteome and phosphoproteome datasets [based on Figure 1I]).

Suppl. Figure 7. Microglial Rac1 modulates single spine Ca^{2+} and actin dynamics.
A, Strategy for studying the impact of microglial Rac1 secretome on neuronal spine Ca^{2+} dynamics and actin polymerization/depolymerization. **B-N,** Primary cortical neuronal cultures co-expressing GCamp6f (representative images in C) and Lifeact-DsRed (representative images in D) were recorded in saline for 10 min and then recorded upon stimulation with conditioned media from primary microglial cultures (MCM) carrying scrambled sequence or Rac1 shRNA. In all conditions, neurons were co-stimulated with 2M KCl. Histograms display linear regressions, and violin plots display median with quartiles (n=88-112 spines pooled across 3 independent neuronal cultures). ****p<0.0001 (unpaired t-test (E and F); ANCOVA (H, I, J, K, L, and M). Scale bars: C: 5 µm; D: 2 µm.

Suppl. Figure 8. Context-dependent synaptic signaling remodeling independent of microglia.
A, Synaptic pathways modulated by experience (EE vs. CE) revealed by phosphoproteomic analyses (n=3-5 Rac1$^{fl/fl}$ mice). The histogram displays the top enriched pathways. **B,** PPI hubs relative to EE vs. CE in Rac1$^{fl/fl}$ mice. The top relevant phosphoproteins (based on A) altered by experience are displayed. **C,** Segregation of synaptic pathways modulated by

experience but not by microglia (n=3-5 mice per group). Histograms display the top enriched pathways.

Fig 1

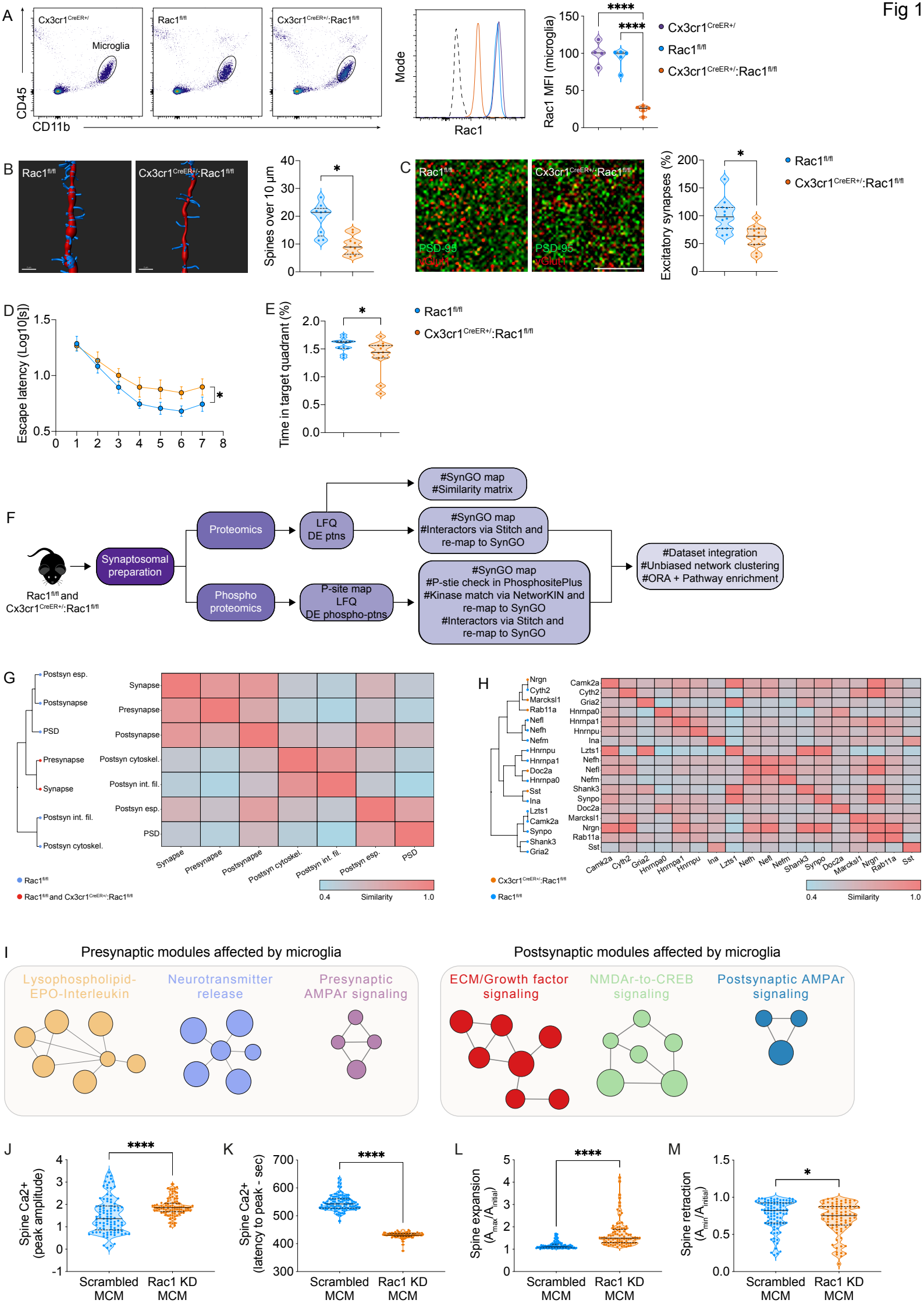
A
Cx3cr1CreER+/
Microglia
Rac1fl/fl
Cx3cr1CreER+/:Rac1fl/fl
CD45
CD11b
Mode
Rac1
Rac1 MFI (microglia)
****
****
Cx3cr1CreER+/
Rac1fl/fl
Cx3cr1CreER+/:Rac1fl/fl
B
Rac1fl/fl
Cx3cr1CreER+/:Rac1fl/fl
Spines over 10 µm
*
C
Rac1fl/fl
Cx3cr1CreER+/:Rac1fl/fl
PSD-95
vGlut1
Excitatory synapses (%)
*
Rac1fl/fl
Cx3cr1CreER+/:Rac1fl/fl
D
Escape latency (Log10[s])
*
E
Time in target quadrant (%)
*
Rac1fl/fl
Cx3cr1CreER+/:Rac1fl/fl
F
Rac1fl/fl and
Cx3cr1CreER+/:Rac1fl/fl
Synaptosomal preparation
Proteomics
Phospho proteomics
LFQ DE ptns
P-site map LFQ DE phospho-ptns
#SynGO map #Similarity matrix
#SynGO map #Interactors via Stitch and re-map to SynGO
#SynGO map #P-stie check in PhosphositePlus #Kinase match via NetworKIN and re-map to SynGO #Interactors via Stitch and re-map to SynGO
#Dataset integration #Unbiased network clustering #ORA + Pathway enrichment
G
Postsyn esp.
Postsynapse
PSD
Presynapse
Synapse
Postsyn int. fil.
Postsyn cytoskel.
Synapse
Presynapse
Postsynapse
Postsyn cytoskel.
Postsyn int. fil.
Postsyn esp.
PSD
Rac1fl/fl
Rac1fl/fl and Cx3cr1CreER+/:Rac1fl/fl
0.4
Similarity
1.0
H
Nrgn
Cyth2
Marcksl1
Rab11a
Nefl
Nefh
Nefm
Hnrnpu
Hnrnpa1
Doc2a
Hnrnpa0
Sst
Ina
Lzts1
Camk2a
Synpo
Shank3
Gria2
Camk2a
Cyth2
Gria2
Hnrnpa0
Hnrnpa1
Hnrnpu
Ina
Lzts1
Nefh
Nefl
Nefm
Shank3
Synpo
Doc2a
Marcksl1
Nrgn
Rab11a
Sst
Cx3cr1CreER+/:Rac1fl/fl
Rac1fl/fl
0.4
Similarity
1.0
I
Presynaptic modules affected by microglia
Lysophospholipid-EPO-Interleukin
Neurotransmitter release
Presynaptic AMPAr signaling
Postsynaptic modules affected by microglia
ECM/Growth factor signaling
NMDAr-to-CREB signaling
Postsynaptic AMPAr signaling
J
Spine Ca2+ (peak amplitude)
****
Scrambled MCM
Rac1 KD MCM
K
Spine Ca2+ (latency to peak - sec)
****
Scrambled MCM
Rac1 KD MCM
L
Spine expansion ($A_{max}/A_{initial}$)
****
Scrambled MCM
Rac1 KD MCM
M
Spine retraction ($A_{min}/A_{initial}$)
*
Scrambled MCM
Rac1 KD MCM

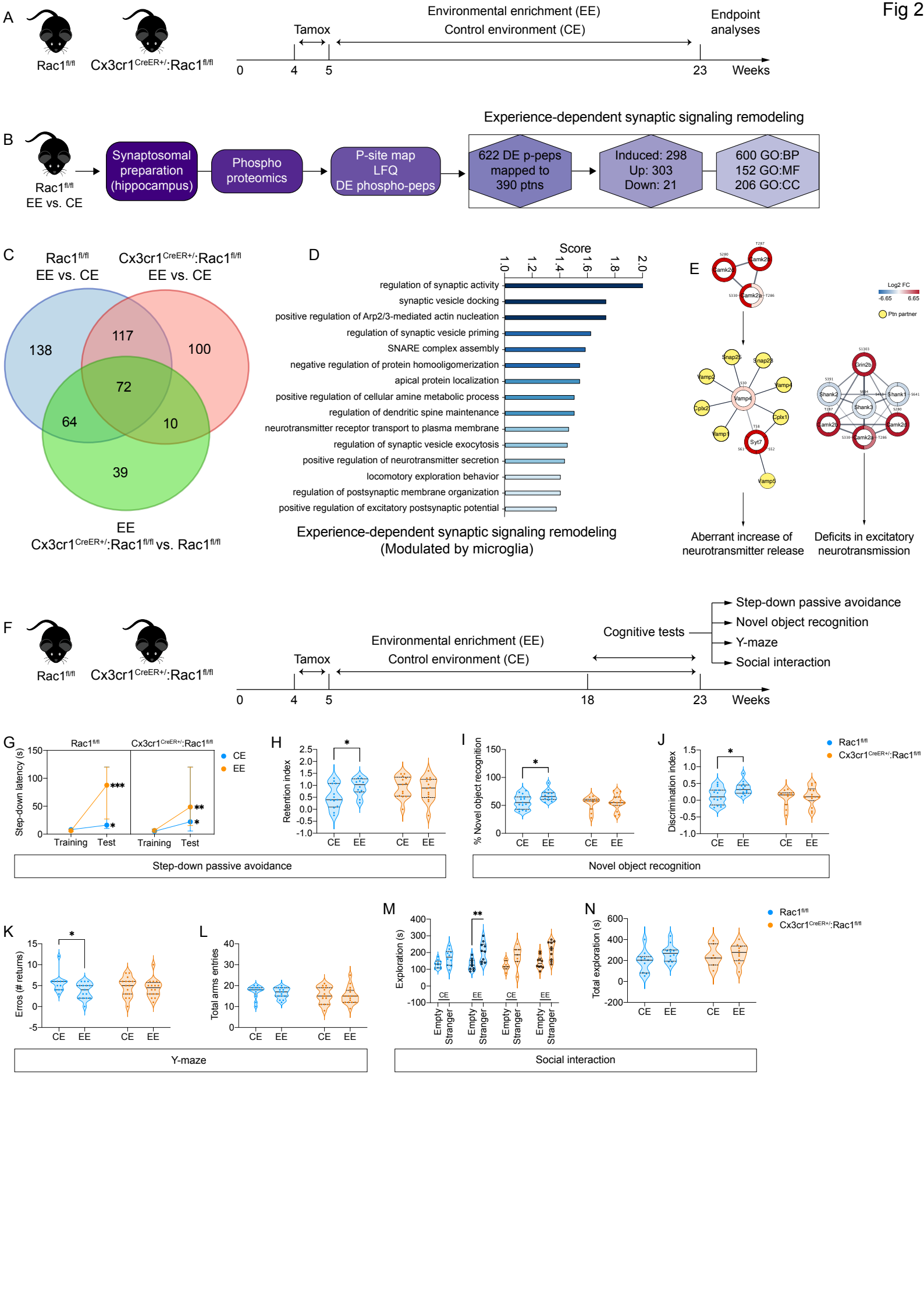
A
Rac1fl/fl
Cx3cr1CreER+/:Rac1fl/fl
Tamox
Environmental enrichment (EE)
Control environment (CE)
Endpoint analyses
0
4
5
23
Weeks
B
Rac1fl/fl
EE vs. CE
Synaptosomal preparation (hippocampus)
Phospho proteomics
P-site map
LFQ
DE phospho-peps
Experience-dependent synaptic signaling remodeling
622 DE p-peps mapped to 390 ptns
Induced: 298
Up: 303
Down: 21
600 GO:BP
152 GO:MF
206 GO:CC
C
Rac1fl/fl EE vs. CE
Cx3cr1CreER+/:Rac1fl/fl EE vs. CE
138
117
100
72
64
10
39
EE
Cx3cr1CreER+/:Rac1fl/fl vs. Rac1fl/fl
D
Score
1.0
1.2
1.4
1.6
1.8
2.0
regulation of synaptic activity
synaptic vesicle docking
positive regulation of Arp2/3-mediated actin nucleation
regulation of synaptic vesicle priming
SNARE complex assembly
negative regulation of protein homooligomerization
apical protein localization
positive regulation of cellular amine metabolic process
regulation of dendritic spine maintenance
neurotransmitter receptor transport to plasma membrane
regulation of synaptic vesicle exocytosis
positive regulation of neurotransmitter secretion
locomotory exploration behavior
regulation of postsynaptic membrane organization
positive regulation of excitatory postsynaptic potential
Experience-dependent synaptic signaling remodeling
(Modulated by microglia)
E
Log2 FC
-6.65
6.65
Ptn partner
Aberrant increase of neurotransmitter release
Deficits in excitatory neurotransmission
F
Rac1fl/fl
Cx3cr1CreER+/:Rac1fl/fl
Tamox
Environmental enrichment (EE)
Control environment (CE)
Cognitive tests
Step-down passive avoidance
Novel object recognition
Y-maze
Social interaction
0
4
5
18
23
Weeks
G
Rac1fl/fl
Cx3cr1CreER+/:Rac1fl/fl
CE
EE
Step-down latency (s)
Training
Test
H
Retention index
I
% Novel object recognition
J
Discrimination index
Step-down passive avoidance
Novel object recognition
K
Erros (# returns)
L
Total arms entries
M
Exploration (s)
Empty
Stranger
N
Total exploration (s)
Y-maze
Social interaction